Oxygen and helium in stripped-envelope supernovae

C. Fremling[1,2], J. Sollerman[1], M. M. Kasliwal[2], S. R. Kulkarni[2], C. Barbarino[1], M. Ergon[1],
E. Karamehmetoglu[1], F. Taddia[1], I. Arcavi[3,4], S. B. Cenko[5,6], K. Clubb[7], A. De Cia[8], G. Duggan[2],
A. V. Filippenko[7,9], A. Gal-Yam[10], M. L. Graham[11], A. Horesh[12], G. Hosseinzadeh[4,3], D. A. Howell[4,3],
D. Kuesters[13], R. Lunnan[1,2], T. Matheson[14], P. E. Nugent[7,15], D. A. Perley[16], R. M. Quimby[17,18], and
C. Saunders[19]

[1] Department of Astronomy, The Oskar Klein Center, Stockholm University, AlbaNova, 10691 Stockholm, Sweden
[2] Department of Astronomy, California Institute of Technology, Pasadena, CA 91125, USA
[3] Las Cumbres Observatory, 6740 Cortona Dr., Suite 102, Goleta, CA 93117, USA
[4] Department of Physics, Broida Hall, University of California, Santa Barbara, CA 93106-9530, USA
[5] NASA Goddard Space Flight Center, Mail Code 661, Greenbelt, MD 20771, USA
[6] Joint Space-Science Institute, University of Maryland, College Park, MD 20742, USA
[7] Department of Astronomy, University of California, Berkeley, CA 94720-3411, USA
[8] European Southern Observatory, Karl-Schwarzschild-Strasse 2, 85748 Garching bei München, Germany
[9] Miller Senior Fellow, Miller Institute for Basic Research in Science, University of California, Berkeley, CA 94720, USA.
[10] Benoziyo Center for Astrophysics, Weizmann Institute of Science, 76100 Rehovot, Israel
[11] Astronomy Department, University of Washington, Box 351580, U.W., Seattle, WA 98195-1580, USA
[12] Racah Institute of Physics, Hebrew University, Jerusalem, 91904, Israel
[13] Institut für Physik, Humboldt-Universität zu Berlin, Newtonstraße 15, 12489 Berlin, Germany
[14] National Optical Astronomy Observatory, 950 North Cherry Avenue, Tucson, AZ 85719, USA
[15] Lawrence Berkeley National Laboratory, 1 Cyclotron Road, MS 50B-4206, Berkeley, CA 94720, USA
[16] Astrophysics Research Institute, Liverpool John Moores University, IC2 Liverpool Science Park, 146 Brownlow Hill, Liverpool, L3 5RF, UK
[17] Department of Astronomy, San Diego State University, San Diego, CA 92182, USA
[18] 9 Kavli IPMU (WPI), UTIAS, The University of Tokyo, Kashiwa, Chiba 277-8583, Japan
[19] Laboratoire de Physique Nucléaire et de Hautes Énergies, Université Pierre et Marie Curie Paris 6, Université Paris Diderot Paris 7, CNRS-IN2P3, 4 place Jussieu, 75252 Paris Cedex 05, France

ABSTRACT

We present an analysis of 507 spectra of 173 stripped-envelope (SE) supernovae (SNe) discovered by the untargeted Palomar Transient Factory (PTF) and intermediate PTF (iPTF) surveys. Our sample contains 55 Type IIb SNe (SNe IIb), 45 Type Ib SNe (SNe Ib), 56 Type Ic SNe (SNe Ic), and 17 Type Ib/c SNe (SNe Ib/c). We compare the SE SN subtypes via measurements of the pseudo-equivalent widths (pEWs) and velocities of the He I $\lambda\lambda 5876, 7065$ and O I $\lambda 7774$ absorption lines. Consistent with previous work, we find that SNe Ic show higher pEWs and velocities in O I $\lambda 7774$ compared to SNe IIb and Ib. The pEWs of the He I $\lambda\lambda 5876, 7065$ lines are similar in SNe Ib and IIb after maximum light. The He I $\lambda\lambda 5876, 7065$ velocities at maximum light are higher in SNe Ib compared to SNe IIb. We have identified an anticorrelation between the He I $\lambda 7065$ pEW and O I $\lambda 7774$ velocity among SNe IIb and Ib. This can be interpreted as a continuum in the amount of He present at the time of explosion. It has been suggested that SNe Ib and Ic have similar amounts of He, and that lower mixing could be responsible for hiding He in SNe Ic. However, our data contradict this mixing hypothesis. The observed difference in the expansion rate of the ejecta around maximum light of SNe Ic ($V_{\rm m} = \sqrt{2E_{\rm k}/M_{\rm ej}} \approx 15{,}000$ km s^{-1}) and SNe Ib ($V_{\rm m} \approx 9000$ km s^{-1}) would imply an average He mass difference of ~ 1.4 M$_\odot$, if the other explosion parameters are assumed to be unchanged between the SE SN subtypes. We conclude that SNe Ic do not hide He but lose He due to envelope stripping.

Key words. supernovae: general – stars: mass-loss – stars: abundances – techniques: spectroscopic

1. Introduction

Stripped-envelope (SE) supernovae (SNe) are thought to be the result of massive stars undergoing core collapse (CC) after the progenitor stars have been stripped of their envelopes to varying degrees. Among SE SNe there are three main subtypes: Type IIb SNe (SNe IIb), Type Ib SNe (SNe Ib) and Type Ic SNe (SNe Ic). Observationally, the dis-

tinction between the subtypes is based on the presence of H and He lines. SNe IIb show helium and hydrogen signatures in early-time spectra, with the hydrogen signatures disappearing over time. SNe Ib show no hydrogen but strong helium features, and SNe Ic show neither hydrogen nor helium lines in their spectra (Filippenko 1997; Gal-Yam 2016). The spectral differences among the SE SN subtypes are typically interpreted as varying amounts of envelope

stripping. SNe IIb progenitors would then have undergone partial stripping, retaining a small part of their hydrogen envelopes. SNe Ib progenitors would be fully stripped of their hydrogen envelopes, and SNe Ic progenitors would be fully stripped of both their hydrogen and helium envelopes.

There are two main mechanisms that can give rise to significant envelope stripping: line-driven winds from isolated massive stars (e.g., Conti 1976; Smith 2014) or binary mass transfer (e.g., Iben & Tutukov 1985; Yoon et al. 2010; Claeys et al. 2011; Yoon 2015). However, alternative explanations for the observed subtypes have been suggested. Enhanced stellar mixing in massive stars could reduce the He Envelope mass by burning it into O, which produces SNe Ic with enhanced O abundances (Frey et al. 2013), and differences in the mixing of ^{56}Ni synthesized in the SN explosions could produce SNe of different observational subtypes from progenitors of otherwise similar structure (Dessart et al. 2012). In the models by Dessart et al. (2012), only SN explosions where the synthesized ^{56}Ni is highly mixed throughout the ejecta, so that the He in the envelope can be nonthermally excited, will produce detectable He lines, as seen in SNe Ib. Models with low mixing become SNe Ic. In these models, higher mixing also results in stronger and faster O I $\lambda7774$[1], and thus SNe Ib would show the strongest and fastest oxygen (see fig. 13 in Dessart et al. 2012).

Observationally, there is some evidence both for and against these scenarios. Piro & Morozova (2014) suggest that up to 1 M$_\odot$ of He could sometimes be hidden in SE SNe, as some objects show very low He velocities indicating that the emitting region lies behind a transparent shell (e.g., the Type IIb SN 2010as; Folatelli et al. 2014). In such objects, based on the calculations by Dessart et al. (2012), the ^{56}Ni synthesized in the explosion might only be mixed into a small part of the He Envelope, resulting in lower velocities measured from absorption minima, and indicating the possibility that even lower mixing, if possible, could produce no He signatures at all (and thus give rise to SNe Ic with very slow expansion velocities). In contrast to this suggestion, it has been found that SNe Ic on average display the highest velocities, followed by SNe Ib, and finally by SNe IIb at the slowest expansion velocities as measured in both the Fe II $\lambda5169$ and the O I $\lambda7774$ absorption lines (Matheson et al. 2001; Liu et al. 2016). However, these results were based on a relatively low number of objects, especially for the O I $\lambda7774$ line. The SNe included in these studies were also discovered mainly in targeted SN searches.

In this paper, we perform an analysis similar to that of Liu et al. (2016), in order to check if their results hold with a larger sample. We investigate He I $\lambda\lambda5876$, 7065 and O I $\lambda7774$ absorption-line strengths and velocities during the photospheric phase for all 176 SE SNe discovered by the Palomar Transient Factory (PTF; Law et al. 2009) and the intermediate PTF (iPTF; Cao et al. 2016; Masci et al. 2017). The PTF and iPTF were untargeted magnitude-limited[2] surveys. Thus, our sample should arguably be less biased compared to previous studies of SE SN spectra that have been mostly based on SNe found via targeted searches[3]. We address the predictions of alternative models for the observed subtypes of SE SNe[4], and compare our results to those found by Matheson et al. (2001) and Liu et al. (2016). Our observations are described in Sect. 2. The methods we have used are presented in Sect. 3, and the results are given in Sect. 4. We search for correlations between the various measurements in Sect. 5. A discussion and our conclusions can be found in Sect. 6.

2. Observations and reductions

2.1. Photometry

To estimate the epoch of maximum light for each SN, we utilize r- or g-band photometry from the Palomar 48 inch (P48) and 60 inch (P60) telescopes, depending on availability for each SN. All photometry has been host-galaxy subtracted. The P60 data were reduced with FPIPE (Fremling et al. 2016), and the P48 data with the PTFIDE pipeline (Masci et al. 2017). The full photometric (i)PTF SE SN sample will be presented in future papers. A subsample has previously been analyzed by Prentice et al. (2016).

2.2. Spectroscopy

During the lifetimes of PTF and iPTF we obtained 507 spectra at unique epochs of SE SNe. We discovered 55 SNe IIb (187 spectra), 45 SNe Ib (125 spectra), 56 SNe Ic (153 spectra), and 17 Type Ib/c SNe (SNe Ib/c; 42 spectra). We have over three times more objects in our sample compared to Liu et al. (2016), who studied 14 SNe IIb, 21 SNe Ib, and 17 SNe Ic. The (i)PTF SE SN spectral sample is summarized in Table 2.

We do not include Type Ic-BL SNe discovered by the (i)PTF in the analysis in this paper; they will be presented by Taddia et al. (in prep.). Hydrogen-poor superluminous SNe (SLSNe) are also excluded. Subsamples of our full spectral dataset have previously been published: some SNe IIb by Strotjohann et al. (2015), iPTF13bvn and PTF12os by Fremling et al. (2014, 2016), iPTF15dtg by Taddia et al. (2016), SN 2013cu (iPTF13ast) by Gal-Yam et al. (2014), PTF12gzk by Horesh et al. (2013), SN 2011dh (PTF11eon) by Arcavi et al. (2011), and SN 2010mb (PTF10iue) by Ben-Ami et al. (2014).

All spectra included in our analysis were reduced using standard pipelines and procedures for each telescope and instrument. The analysis in this paper is focused on the optically thick photospheric phase (we do not analyze spectra taken later than 60 d past maximum light). Normalized spectra limited to the regions around the absorption features used in our analysis will be made available in

---

[1] When discussing this line we effectively refer to the O I $\lambda\lambda7771$, 7774, 7775 triplet.
[2] Approximately 20.5 and 21 mag in the Mould R and Sloan g bands, respectively.

[3] This is potentially important since (i)PTF could find SE SNe in hosts with very low metallicity compared to the average for SE SNe (e.g., Sanders et al. 2012). Two examples are iPTF15dtg (Taddia et al. 2016) and PTF11mnb (Taddia et al. 2017). However, their spectra are similar to those of normal SNe Ic, and we do not find any significant differences in our results compared to Matheson et al. (2001) and Liu et al. (2016). Thus, a detailed analysis of the impact of (i)PTF being untargeted was not performed.
[4] By comparing observed spectra to the models by Dessart et al. (2012), as was previously done by Liu et al. (2016).

electronic form via WISeREP[5] (Yaron & Gal-Yam 2012) and the Open Supernova Catalog[6] (OSC; Guillochon et al. 2017). A catalogue paper that will present full spectra is in preparation.

3. Data analysis and methods

3.1. Time of Maximum Light Estimates

We estimate the time of maximum light for each SN in our sample using the observed light curves (LCs), by performing template fits to the r-band LC of each object (or the g-band LC if r is not available). When fitting the LCs we allow for a shift and stretch of the templates. The LC peaks of SNe IIb were estimated using the r-band LC of SN 2011dh (Ergon et al. 2014). The LC peaks of SNe Ib and Ic were estimated using the LC templates by Taddia et al. (2015).

The time of maximum light was used to calculate the rest-frame epochs of our spectroscopic observations (see Table 2). Throughout this paper we use the convention that negative epochs refer to epochs before maximum light (e.g., -5 d) and positive epochs refer to past maximum (e.g., $+5$ d). For objects where it was not possible to determine the time of maximum light, we use the spectra obtained by the (i)PTF to classify them (see Table 2), but do not include them in any further analysis.

3.2. Spectral Classifications

To classify the SNe in our sample we have used SNID (Blondin & Tonry 2007) with template spectra constructed from the SE SNe in the Harvard-Smithsonian Center for Astrophysics sample (Modjaz et al. 2014; Liu & Modjaz 2014). The full spectral sequence for each SN has been run automatically through SNID, and the subtype with the most matches across the spectral sequence (before $+60$ d) is used to classify the SN.

If there are several conflicting matches for different spectra of the same SN, or if there is a similar number of matches for two subtypes for a certain spectral sequence, the results are manually inspected both in SNID and by inspecting the regions around $H\alpha$, $H\beta$, and He I $\lambda\lambda5876, 7065$; if the best SNID matches change over time from SNe IIb to SNe Ib, or if both $H\alpha$ and $H\beta$ absorption is detected at a similar velocity in any early-time spectrum, we classify the object as a SN IIb. Furthermore, if manual inspection is needed, H is undetected, and absorption from both of the He I $\lambda\lambda5876, 7065$ lines is detected, we classify the object as a SN Ib; if neither H nor He is detected, the object is classified as a SN Ic (see also Shivvers et al. 2017, who also discuss the difficulty of classifying some SE SNe).

SNe with spectra where the signal-to-noise ratio (SNR) is not sufficiently good to distinguish a SN Ib from a SN Ic, or where the classification remains ambiguous after manual inspection, are classified as SNe Ib/c. These are not included in our analysis, except to check for the impact on average values (Sect. 4) and correlations (Sect. 5) by including these objects in both the SN Ib and SN Ic groups and redoing the calculations. We find no significant changes in any of our conclusions by doing this exercise.

3.3. Pseudo-Equivalent Widths

To estimate the strength of absorption features in our spectra we utilize the pseudo-equivalent width (pEW; e.g., Nordin et al. 2011), defined as

$$\mathrm{pEW} = \sum_{i=1}^{N} \left(1 - \frac{f(\lambda_i)}{f_0(\lambda_i)}\right) \Delta\lambda_i, \qquad (1)$$

where λ_1 and λ_N define the estimated extent of the absorption feature ($\lambda_1 < \lambda_N$), and $f_0(\lambda_i)$ is the continuum, estimated as a linear fit to the data surrounding λ_1 and λ_N.

We follow similar principles as Liu et al. (2016) when choosing the endpoints of the absorption features and where to measure the continuum levels. First, we smooth the spectrum[7] around the absorption feature. The first peak on the blue side of the feature is then chosen as λ_1 and the peak closest to the expected position for the relevant emission-line peak in the rest frame is chosen as λ_N. Typical results of this method are shown for an example spectrum taken close to maximum light for each SE SN subtype in Fig. 1 (we show Type Ib iPTF13bvn, data from Fremling et al. 2014; Type IIb SN 2011dh[8], data from this work; and Type Ic PTF10osn, data from this work). Note that if there are multiple peaks within ~ 100 Å of the apparent ends of the absorption feature, we choose the peaks that give the highest pEW value as λ_1 and λ_N (see feature 1 in the spectrum of SN 2011dh in Fig. 1). In the case where there is no clear peak on the blue side of the absorption feature, we limit the pEW measurement in velocity space to no larger than $25,000$ km s^{-1} for the position of λ_1. If there is no clear absorption feature and no clear emission peak to use as λ_N (typical especially for the He I $\lambda7065$ position in SNe Ic), we fix λ_N at the expected rest-frame position of the emission feature and set λ_1 where the value of pEW is maximized while λ_1 is below the maximum allowed velocity (see feature 2 in the spectrum of PTF10osn in Fig. 1).

Uncertainties in the pEW measurements are estimated using a Monte-Carlo method. First, we create a local measurement of the noise by dividing the original spectrum with a heavily smoothed spectrum and computing the standard deviation locally (in a region of about 1000 Å) around the position of the absorption feature to be measured. Next, we create many simulated noisy spectra by adding noise using a Gaussian distribution and the standard deviation. The pEW measurement is then repeated on each simulated spectrum and the standard deviation of the results is taken as the 1σ uncertainty of our measurements. In this procedure, we also randomly change the continuum endpoints in each simulated spectrum within a 25 Å region to account for possible uncertainties in the identifications of the peak positions of the spectral features. Although this is not necessary for good-quality spectra with accurate peak position estimates, we still perform the same calculation regardless of the spectral quality for consistency[9].

3.4. Expansion Velocities

To estimate expansion velocities we use the minima of the identified absorption features in our pEW measurements. This is done by fitting a polynomial to the absorption feature and locating the minimum of the fit[10]. Example fits are shown in Fig. 1 (dashed black lines). Uncertainties are estimated using a similar MC approach as for the pEW measurements. The minimum of each simulated spectrum is estimated by polynomial fits, and the standard deviation is taken as the 1σ uncertainty of our velocity measurements.

4. Results

4.1. Absorption Strengths

The method we use to measure pEWs (Sect. 3.3) will by construction tend to give positive values for features 1 and 2 as identified in Fig. 1 for all SE SN spectra, including those of SNe Ic. In SNe IIb and Ib, these features are typically identified as He I $\lambda\lambda5876, 7065$. However, positive pEW measurements in a SN Ic does not necessarily mean that He is present in the ejecta. Our method simply maximizes the pEW measurement of any absorption from any line that could give rise to a feature in these regions of the spectrum. Possible contamination for the He I $\lambda5876$ absorption line is Na I D, and for He I $\lambda7065$, Al II (e.g., Kasliwal et al. 2010). Regardless, throughout this paper we will refer to any measurable absorption found at the position of features 1 and 2 as potential He I $\lambda\lambda5876, 7065$ absorption, even for SNe Ic, to simplify the discussion.

4.1.1. Helium

We show the individual He I pEW measurements of the SNe IIb, Ib, and Ic included in our sample in the top panels of Fig. 2. The evolution of the mean values and the standard deviation of the means of each subtype is shown in the middle panels of the figure.

Similar to Liu et al. (2016), we find that SNe Ib show larger pEW values on average compared to SNe IIb for the He I $\lambda5876$ feature before +20 d, after which the pEW values become similar. The probability that this difference is not real based on a two-sample Kolmogorov-Smirnov (K-S) test is $p < 0.03$, when we consider the measurements between −10 to +10 days of each subtype. For the same time interval we show the cumulative distribution functions (CDFs) of the pEW values for each subtype in the bottom-left panel of Fig. 2. SNe Ic show significantly weaker absorption in this line at early times ($p < 0.001$, before +20 d when compared to both our SN IIb and Ib). However, the pEW values of SNe Ic become more similar to those of the other SE SNe after +30 d. This is likely a result of contamination from Na I gradually becoming more significant, although a weak contribution from He I cannot be ruled out.

In contrast to Liu et al. (2016), we do not find a strong difference between SNe IIb and Ib for the pEW values of the He I $\lambda7065$ absorption line at epochs past $\sim +40$ d (see the middle panels of our Fig. 2 and compare to fig. 6 in Liu et al. 2016). Instead, we find that SNe IIb and Ib are remarkably similar during all epochs when we could obtain

---

[10] We use polynomials of degree 4 to 7 depending on the feature shape and quality of the spectrum.

Table 1: Weighted mean values for SE SNe at maximum light.

SN Type	pEW (O I $\lambda7774$) (Å)	v (He I $\lambda5876$) (km s^{-1})	v (O I $\lambda7774$) (km s^{-1})
SNe Ic	70 ± 15	...	9800 ± 600
SNe Ib	28 ± 12	9500 ± 600	7900 ± 600
SNe IIb	32 ± 10	8000 ± 500	7000 ± 500

Note. — Uncertainties are given as the standard deviation of the mean values, $\sigma/\sqrt{N}$, where N is the number of objects included in the calculation.

meaningful averages based on measurements of multiple objects (see the bottom-right panel of Fig. 2 for the CDFs for the −10 d to +10 d time interval). In a K-S test we do not find any statistically significant difference among our SNe IIb and Ib in He I $\lambda7065$ at any time. Our sample contains several SNe Ib that evolve toward much stronger absorption in this line compared to those studied by Liu et al. (2016). We also have several SNe IIb showing weaker absorption than those studied by Liu et al. (2016). This could be due to the fact that the (i)PTF is untargeted, resulting in a greater diversity of objects, or a consequence of our larger sample size.

SNe Ic show consistently much weaker pEW values measured at the expected position for He I $\lambda7065$ absorption at all times, although we do observe a rising trend over time in the pEW values that is similar to that of the other subtypes. This could be evidence for a small residual He envelope in some SNe Ic (but see also Sect. 5.1 and Fig. 5). It could also be due to contamination from the nearby [Fe I] $\lambda7155$ line that is gradually getting more significant, or to Al II absorption.

4.1.2. Oxygen

Absorption-strength estimates of the O I $\lambda7774$ line are shown in the top-left panel of Fig. 3. We find that before +20 d, SNe Ic clearly show the highest pEW values, with no detectable difference between SNe IIb and Ib. The pEW distribution we find for SNe Ic is different from both our SN IIb and SN Ib distributions, with $p < 0.001$ in a two-component K-S test in both cases, when measured in the interval −10 d to +10 d. There is no statistically significant difference between SNe IIb and Ib for any time interval. The evolution of the mean value for each class is displayed in the top-right panel of Fig. 3, showing that SNe Ic are on average stronger in this line compared to other SE SNe by almost a factor of two. The CDFs of the subtypes are shown in the bottom panel of Fig. 3. Before peak there are very few SNe IIb and Ib with pEW values higher than 60 Å. Thus, a single pEW measurement of O I $\lambda7774$ on an early-time spectrum can be used to classify SNe Ic (see also Sun & Gal-Yam 2017).

Past +40 d, there is no statistically significant difference between the pEW values of any of the SE SN subtypes. However, at these later epochs the measurements become difficult owing to increasingly strong emission lines of [Ca II] $\lambda\lambda7293, 7325$ that affect the continuum typically used to measure the O I $\lambda7774$ absorption. The similarity among the subtypes at later epochs could be a result of this contamination. Table 1 lists the weighted mean pEW for the O I $\lambda7774$ absorption feature for each SE SN subtype at maximum light.

4.2. Velocities

Typically, the Fe II $\lambda5169$ line is used as a tracer for the expansion velocity of the SN photosphere in SE SNe (Dessart & Hillier 2005). The photospheric expansion velocity, measured in this way, can be used for LC modeling (e.g., Arnett 1982), and sample studies of SE SN LCs have in general followed this methodology (e.g., Drout et al. 2011; Cano 2013; Taddia et al. 2015; Lyman et al. 2016; Prentice et al. 2016). However, Dessart et al. (2015) have shown that the notion of a photosphere in SE SNe is ambiguous. Instead, Dessart et al. (2016) suggest that it is more appropriate to estimate the mean expansion rate via the absorption minimum of the He I $\lambda5876$ line for SNe IIb and Ib, and the O I $\lambda7774$ absorption minimum in SNe Ic. Expansion-velocity measurements based on these lines are presented below (average expansion velocities around maximum light can be found in Table 1).

4.2.1. Helium

Expansion-velocity measurements obtained from the minimum of the He I $\lambda5876$ absorption line for the SNe IIb and Ib in our sample are shown in the top-left panel of Fig. 4. For SNe Ic, we find that very few objects show velocities that could be consistent with He I, and there is generally a very large scatter in our measurements (since He is likely not detected). Thus, we do not include results for SNe Ic in this figure or in Table 1.

SNe Ib tend to be faster, on average, compared to SNe IIb in this line (see the middle-left panel of Fig. 4). Averages obtained from the absorption minimum of the He I $\lambda7065$ line (overplotted as thick solid lines in the middle-left panel of Fig. 4) give similar results as for the He I $\lambda5876$ line. These findings are consistent with the result by Liu et al. (2016).

Around maximum light the average He I $\lambda5876$ absorption velocity of our SNe Ib is $\sim 9500 \pm 600$ km s^{-1}. For SNe IIb we measure 8000 ± 500 km s^{-1}. In a two-component K-S test we find that the SN Ib velocity distribution differs from the SN IIb distribution with $p < 0.004$ for the null hypothesis (calculated between -10 d and $+10$ d; see also the CDFs in the bottom-left panel of Fig. 4).

4.2.2. Oxygen

Velocity estimates based on the absorption minimum of the O I $\lambda7774$ line are shown in the top-right panel of Fig. 4. We find clear evidence for SNe Ic on average being faster compared to SNe IIb and Ib, with a few SNe Ic showing very high velocities at early times, followed by a rapid decline ($> 18,000$ km s^{-1} before peak; e.g., PTF12gzk; Ben-Ami et al. 2012; Horesh et al. 2013). A similar result was found by Liu et al. (2016). However, their weighted averages at maximum light were based on only 7 SNe Ic and 4 SNe Ib. If we consider the time interval of -2 d to 2 d, we have velocity estimates of 14 SNe IIb, 8 SNe Ib, and 22 SNe Ic. In a two-component K-S test for the velocity distributions between -10 d and $+10$ d, we find that SNe Ic differ from both SNe IIb and Ib with $p < 0.01$ for the null hypothesis. Even if we exclude the 5 fastest SNe Ic in our sample, we still find a significantly higher average velocity for the remaining SNe Ic (this can be seen clearly in the CDFs; bottom-right panel of Fig. 4). In the middle-right panel of

Fig. 4 we also overplot the average He I $\lambda5876$ absorption velocity for SNe Ib as a thick solid line. The velocities derived from this line in SNe Ib evolve in a very similar way as the O I $\lambda7774$ absorption velocities in SNe Ic.

Compared to the SNe studied by Liu et al. (2016), there is somewhat more diversity in our SN Ib sample; we have a few SNe Ib at rather high velocities ($> 10,000$ km s^{-1} around peak brightness). We have also performed velocity measurements of O I $\lambda7774$ for our SNe IIb, and find that these tend to be slightly slower compared to our SNe Ib (with a few objects showing velocities < 5000 km s^{-1}). However, the difference between the SN IIb and SN Ib distributions is not statistically significant in a K-S test ($p < 0.19$), when measured between -10 d and $+10$ d.

5. Correlations

To further probe the spectral characteristics of the SE SN subtypes, we have searched our sample for correlations among the measured quantities (pEWs and velocities). However, both pEWs and velocities evolve with time. Thus, to minimize the impact of the time dependencies, we restrict ourselves to comparing average values for restricted time intervals. In our search we computed all correlations (Pearson's r-values and corresponding p-values) for all possible (1 d integer shifted) time bins of 10 d width starting from -20 d to $+50$ d. In all cases where we find statistically significant correlations, we find that at least 10 adjacent time bins give similar correlation coefficients and statistically significant p-values. In several cases, the interval $+10$ d to $+20$ d gives particularly clear correlations.

We have also investigated the possible impact of slightly different temporal evolutions among the SNe. Objects with slower evolving LCs could take more time to reach peak absorption strengths, for example, in their He lines. To simulate the effect of this, we have stretched the spectral sequence of SN 2011dh in time, following a Gaussian distribution that corresponds to the observed LC stretch values of the (i)PTF SE SN sample. We find that the potential impact from this effect is not enough to be the main cause of any of our correlations. We find no observational correlations between absorption strength or velocity and LC broadness, except for a few objects with very large stretch values (marked with yellow diamonds in Figs. 5 and 6). The statistical significances of the correlations shown in Fig. 5 and Fig. 6 are not affected by including or excluding these objects from the calculations.

5.1. The Helium Shell

We find that there is a correlation between the pEWs of He I $\lambda7065$ and He I $\lambda5876$ (top-left panel of Fig. 5; measured by computing the average pEW between $+10$ d and $+20$ d for each SN). There is a large scatter, but the trend appears to be the same for both SNe IIb and Ib, and we get $r = 0.66$ and $p < 0.001$, when combining the values of SNe IIb and Ib. There is no statistically significant correlation for SNe Ic ($r = 0.48$, $p < 0.12$). This supports an interpretation where both of these lines are dominated by He in SNe IIb and Ib but not in SNe Ic. The latter is also indicated by the difficulty in obtaining a velocity estimate for He I $\lambda5876$ for SNe Ic (Sect. 4.2.1). For Type Ic SNe there is a large spread in the pEWs

of He I $\lambda 5876$, but not in He I $\lambda 7065$. This could indicate that Na I contamination is quite significant and might be causing most of the scatter (see, e.g., Dessart et al. 2015). A linear fit that excludes SNe Ic gives the relation $\mathrm{pEW}_{\lambda 5876} = 30(\pm 17) + 1.3(\pm 0.3) \times \mathrm{pEW}_{\lambda 7065}$ [Å], consistent with a 1:1 relation. Furthermore, we find that the trend is similar when calculated for any time interval of similar duration between -10 d and $+50$ d.

In the top-left panel of Fig. 6 we show the average velocity vs. the average pEW of the He I $\lambda 7065$ absorption line measured between $+10$ d and $+20$ d. For SNe IIb and Ib there is a decreasing trend, with higher velocities giving weaker absorptions ($r = -0.63$, $p < 0.001$). This is what would be expected for He shells of lower mass being accelerated to higher velocities, assuming similar kinetic energies in the SN explosions. We find a similar trend for the He I $\lambda 5876$ line during the same time interval (not shown). The trend in He I $\lambda 7065$ is statistically significant when the averages are calculated for all intervals starting from -10 d and ending at $+40$ d. Prior to -10 d, the signatures from He I $\lambda 7065$ are generally very weak (see Fig. 2).

5.2. The Oxygen Shell

To probe the oxygen-absorbing region of the ejecta, we compare the average pEW calculated between $+25$ d and $+45$ d for O I $\lambda 7774$ vs. He I $\lambda 7065$ (right panel of Fig. 5). For both SNe IIb and Ib there is an increasing trend with objects showing stronger O I $\lambda 7774$ features also having stronger He I $\lambda 7065$ ($r = 0.73$, $p < 0.001$ when SNe IIb and Ib are combined). A linear fit, excluding SNe Ic, gives a relation consistent with $\mathrm{pEW}_{\lambda 7065} = 1.0 \times \mathrm{pEW}_{\lambda 7774}$. For the SNe Ic in Fig. 5, we find no statistically significant correlation between the pEWs. The pEW of He I $\lambda 7065$ is always low, but it can be associated with a wide range of pEWs of O I $\lambda 7774$. For time intervals earlier than $+20$ d, the trend for SNe IIb and Ib disappears, and around peak brightness the pEWs appear to be randomly scattered.

In the top-right panel of Fig. 6 we show the average velocity against the average pEW of the O I $\lambda 7774$ absorption line measured between $+10$ d and $+20$ d. SNe IIb and Ib are scattered with no apparent correlations at lower absorptions and velocities compared to the SNe Ic in our sample (although there are a few outliers among all three subtypes). For SNe Ic there is a decreasing trend, with higher velocities corresponding to weaker absorptions ($r = -0.50$, $p < 0.024$). Similarly as what we found for the He shell, this could indicate that we are observing O shells of lower mass being accelerated to higher velocities. The lack of such a trend for SNe Ib and IIb would be expected, since the O absorbing region is located rather deep inside the ejecta behind significant amounts of He during this phase.

In the bottom panel of Fig. 6 we show the average velocity of the O I $\lambda 7774$ absorption line vs. the average pEW of the He I $\lambda 7065$ absorption line, measured between -10 d and $+10$ d for SNe IIb, Ib, and Ib/c; for SNe Ic, the average pEW/2.2 of O I $\lambda 7774$ vs. O I $\lambda 7774$ velocity is shown. SNe IIb and Ib that exhibit fast O (> 8000 km s^{-1}) also show weak He absorption ($r = -0.65$, $p < 0.001$). To show weak He absorption, we must have faster He (the top-left panel of Fig. 6). These findings, taken together, suggest that to see strong and fast O (i.e., the SNe Ic in our sample), the He envelope must have been physically removed. The

trend seen for SNe IIb and Ib is consistent with the trend in pEW vs. velocity of O I $\lambda 7774$ in SNe Ic, if the pEW is scaled down by a factor of 2.2. This suggests that the stripping does not necessarily stop as the He envelope is lost; some SNe Ic could be experiencing significant stripping of material from their C-O cores. Higher kinetic energy could also explain the higher velocities in SNe Ic, but it is difficult to explain why this would simultaneously lead to lower pEWs (see Sect. 6 for further discussion).

6. Discussion and Future Outlook

The pEWs and velocities we have measured are generally consistent with those previously reported by Matheson et al. (2001), Liu et al. (2016), and Prentice & Mazzali (2017)[11]. SNe Ic are faster and show stronger O pEWs in early-time spectra compared to the other SE SN subtypes, He pEW is anticorrelated with He and O velocities for SNe IIb and Ib, and O pEW appears anticorrelated with O velocity for SNe Ic. LC sample studies show no robust evidence for larger average ejecta masses or explosion energies in SNe Ic, compared to SNe IIb and Ib, that could result in faster and stronger oxygen signatures. Therefore, we agree with Matheson et al. (2001) and Liu et al. (2016); in order to have fast and strong O absorption at early times in most SNe Ic, the simplest explanation would be that we are immediately seeing into their C-O cores; their H and He envelopes have been physically removed prior to the explosions due to stellar winds or binary mass transfer.

However, models by Dessart et al. (2012) suggest that differences in $^{56}\mathrm{Ni}$ mixing could give rise to both SNe Ic and Ib, from similar progenitors with significant He envelopes ($\sim 1.5\,\mathrm{M}_\odot$). In these models SNe Ic have low mixing, so that the radioactive $^{56}\mathrm{Ni}$ is never close enough to nonthermally excite the He in the envelope. Conversely, SNe Ib must have highly mixed $^{56}\mathrm{Ni}$, in order to display observable He lines. A consequence of the lower mixing in these models is narrower and weaker absorption lines, along with lower velocities measured from absorption minima (especially for the O I $\lambda 7774$ absorption; see fig. 13 in Dessart et al. 2012). Thus, the results by Dessart et al. (2012) can be interpreted such that, if different $^{56}\mathrm{Ni}$ mixing is the main difference between the SE SN subtypes, SNe Ic should on average show both slower and weaker O I $\lambda 7774$ absorption.

Our results are not consistent with such low mixing models; for the SNe Ic in our sample we find on average both stronger O I $\lambda 7774$ absorption (Fig. 3) and faster velocities (Fig. 4) at early times. Liu et al. (2016) used a comparable result to argue against low-mixing models for SNe Ic, with the supporting evidence that LC studies show that SNe Ib and Ic seem to have progenitors of similar mass[12]. However, if SNe Ic came from higher energy explosions and significantly more massive progenitors compared to SNe Ib, the result could be higher kinetic energies in the C-O layer, consistent with stronger and faster O signatures. Furthermore, if the $^{56}\mathrm{Ni}$ is not significantly mixed into the outer He envelopes, there will be no He signatures, and models for the

---

[11] This study was based largely on the same sample as Liu et al. (2016), and the results are consistent between the two papers for the He line strengths and velocities. The O lines were not analyzed by Prentice & Mazzali (2017).

[12] With progenitors of similar mass, the stronger O signatures in SNe Ic would be explained by a lack of a He envelope.

bolometric LC will underestimate the total ejecta masses (and the derived progenitor masses for SNe Ic), since the outer parts of the envelope devoid of ^{56}Ni would not contribute to the LC (Piro & Morozova 2014). Anderson et al. (2012) suggested that SNe Ic prefer younger stellar populations, which could be consistent with larger progenitor masses (> 30 M$_\odot$). LC studies also suggest that the most massive SE SNe could have higher explosion energies (e.g., Lyman et al. 2016). Thus, low-mixing models for SNe Ic cannot easily be ruled out based on just a comparison of average O strengths and velocities among the subtypes.

To address this issue we looked for correlations among the quantities we have measured (Sect. 5). In particular, we found that there is an anticorrelation between He pEW and O velocity for SNe Ib and IIb, as well as between O pEW and velocity in SNe Ic (bottom panel, Fig. 6). To explain this behavior with models with gradually increasing kinetic energy (progenitor mass), and ^{56}Ni mixed in such a way that the He gradually disappears, would require a significant amount of fine-tuning. The nickel mixing would have to decrease drastically as the kinetic energy increases, which seems counterintuitive since higher velocity ejecta imply higher velocity ^{56}Ni. The alternative to this complicated scenario would be that the He envelope is gradually stripped off — a much more elegant solution. Thus, we conclude that He most likely is not hidden in SNe Ic due to low mixing[13]. Furthermore, early LC studies of SE SNe indicate that the ^{56}Ni mixing appears to be high among all SE SN subtypes (Taddia et al. 2015), and possibly the highest for SNe Ic. Thus, models for normal SNe Ic should have high mixing, similar to the level of mixing needed for good spectral matches to SNe Ib.

If He cannot be hidden in typical SE SNe due to mixing, the anticorrelation between He pEW and O /He velocities in Fig. 6 suggests that envelopes with a wide range of He masses or abundances can be present at the time of explosion, since there appears to be a continuum from SNe Ib to Ic in this phase space (top-left panel, Fig. 6). This could be due to progenitors from a range of initial masses undergoing a similar amount of stripping, or a continuum in the amount of stripping experienced by the progenitor stars, or a combination thereof[14]. Furthermore, if higher mixing or kinetic energies were the cause of the increasing O I $\lambda7774$ velocities from SNe Ib to Ic, there is no clear explanation why the He lines would disappear as the mixing or kinetic energy increases. For very high velocities ($\gtrsim 20,000$ km s^{-1}), spectra do become gradually more featureless (like SNe Ic-BL), and it would be difficult to measure pEWs following our prescription (Sect. 3.3); but we are here dealing with much lower velocities ($\lesssim 10,000$ km s^{-1}). From the models by Dessart et al. (2016), it is also clear that varying the kinetic energy, within typical ranges for SE SNe, will not change the observed SN type from a SN Ib to a SN Ic.

In particular, we find that the relation for the pEW of He I $\lambda7065$ and the O I $\lambda7774$ velocity in SNe IIb and Ib can be fit by pEW$\propto v^{-2}$ (Fig. 6). This suggests that there could

be a simple relation between absorption strength and the mass of the He envelope in SE SNe, since $M_{ej} \propto E_k/v_{ph}^2$ (Arnett 1982). If we assume that E_k remains unchanged as the velocity increases, and scale this relation so that the O I $\lambda7774$ velocity predicted for a total ejecta mass of 2.1 M$_\odot$ is 4900 km s^{-1} to match the observed velocities and masses of SN 2011dh (PTF11eon) and PTF12os (Fremling et al. 2016), we find that to turn these SNe IIb into SNe Ic[15], roughly 1.0–1.6 M$_\odot$ of He would have to be removed (see the dashed vertical lines in the bottom panel of Fig. 6). This is consistent with the He envelope mass used in spectral models of SN 2011dh (e.g., Jerkstrand et al. 2015). Modeling work also clearly shows that a range of He envelope masses produces He signatures of various strengths (see, e.g., figure 11 in Hachinger et al. 2012). However, the exact relationship between He absorption pEW and He envelope mass has not been investigated. We strongly encourage future modeling efforts in this direction. Since the anticorrelation between He pEW and O velocity for SNe IIb and Ib is consistent with the behavior of O pEW and velocity in SNe Ic, our data also support the idea that some SE SNe can experience significant stripping all the way into their C-O cores[16].

Dessart et al. (2016) have suggested that the best way to constrain the explosion parameters (e.g., total kinetic energy and ejecta mass) for SE SNe is to use the expansion rate of the ejecta ($V_m = \sqrt{2E_k/M_{ej}}$) derived from the He I $\lambda5876$ absorption line for SNe IIb and Ib and from the O I $\lambda7774$ line for SNe Ic, instead of v_{ph} in the Arnett (1982) model. If we assume that the average kinetic energy among the SN Ib and Ic subtypes is the same, we can use the observed He I and O I velocities for SNe Ib and Ic at maximum light (see Table. 1 and the middle-right panel of Fig. 4) to roughly estimate what mass difference these velocities would imply for these subclasses, which could be interpreted as the average mass of the He envelope that is lost in a SN Ic. Using the relation between the ejecta mass (M_{ej}) and the kinetic energy (E_k) for a constant density sphere expanding homologously (e.g., Lyman et al. 2016),

$$\frac{5}{3}\frac{2E_k}{M_{ej}} = v_{ph}^2, \qquad (2)$$

we find with[17] $V_{m-Ib} = (9500-2640)/0.765 \approx 9000$ km s^{-1}, $V_{m-Ic} = (9800 - 2990)/0.443 \approx 15,000$ km s^{-1}, $E_k = 1 \times 10^{51}$ erg, and $M_{ej-Ib} = 2.1$ M$_\odot$, that the V_m difference can be reproduced by removing 1.4 M$_\odot$ of material from the envelope for an average SN Ib (note the similarity to the result based on the O velocity for SN 2011dh above). However, these calculations hold only if E_k really is the same (on average) between the subtypes. This is not necessarily the case; binary models of SE SNe typically require slightly higher initial masses to produce SNe Ic compared to SNe Ib (Yoon 2015). Thus, SNe Ic could have slightly larger C-O cores, and higher kinetic energies, so that the final ejecta masses derived from bolometric LC fitting end

---

[13] See also Hachinger et al. (2012), who have shown that more than ~ 0.1 M$_\odot$ of He cannot be hidden in highly mixed SE SN models.

[14] Since the transition in He pEW from SNe Ib to SNe Ic is continuous, there is a range where making the distinction between these subtypes can be ambiguous and dependent on the quality of the spectra (see Liu et al. 2016; Shivvers et al. 2017, for further discussion).

[15] In terms of reaching typical SN Ic O I $\lambda7774$ velocities between +10 d and +20 d, which are 6000 to 10,000 km s^{-1}, for 66.7% of the SN Ic population.

[16] See, e.g., SN 2005ek, possibly the result of mass transfer from a He star to a compact companion in a very close binary (Drout et al. 2013; Tauris et al. 2013).

[17] V_m relations from Dessart et al. (2016).

up very close to those of SNe Ib. This could affect our estimate of the average He mass that is lost in a SN Ic, but the anticorrelations we have found between pEW and velocity for both He and O cannot easily be explained without removing mass from the envelopes. Spectral modeling efforts in combination with hydrodynamical modeling are needed in order to make more quantitative statements.

Piro & Morozova (2014) suggested that SN 2011dh and iPTF13bvn could have a significant amount of transparent He , based on their low He absorption velocities (which would result in underestimated ejecta masses derived from their LCs). We do find low velocities in these SNe. However, at the same time, they show some of the strongest He I $\lambda\lambda5876, 7065$ absorption features in our sample (see, e.g., the bottom panel of Fig. 6). This would not be expected if only a small inner part of the He envelope is producing the observed He lines. In the top-left panel of Fig. 6 there are only two SNe IIb at velocities lower than ~ 7000 km s^{-1} that also show low pEWs. Thus, while this effect could be present in a few objects, it does not appear to be dominating. We also found that SNe Ib and IIb show a trend with high He pEW values correlated to low velocities (see Fig. 6). This is also inconsistent with partly transparent He envelopes being typical for these subtypes; we would expect to have more objects at both low pEW and low velocity (only a small part of the He envelope is emitting, and it should be slow since the emitting region would be located behind an outer transparent envelope of significant mass).

There are two SNe IIb (PTF10qrl and iPTF15cna) in our sample that show weak He I $\lambda7065$ absorption, along with very low O I $\lambda7774$ velocities (bottom panel of Fig. 6). At the same time, their LCs are very broad (stretched by a factor of ~ 2, compared to SN 2011dh; Karamehmetoglu et al., in prep.). This indicates that they likely come from massive progenitor stars ($\gtrsim 30$ M$_\odot$). For such progenitors, even models with high mixing can have difficulties in producing He signatures, since the He envelope is far from the center of the explosion outside a large C-O core (Dessart et al. 2015; Dessart et al. 2016). In these models there is some transparent helium, leading to weak or no He signatures, along with low expansion velocities of O I $\lambda7774$ (since the O is slowed down by a significant He envelope), consistent with our observations of these two SNe. These objects can also be used as an argument against the suggestion by Frey et al. (2013) that very massive stars ($\gtrsim 23$ M$_\odot$) would all become SNe Ic with enhanced O abundances in their outer envelopes owing to strong stellar mixing. The top-right panel of Fig. 6 shows that the majority of SE SNe with broad LCs do not exhibit significantly enhanced O absorption.

Going forward, we are in the process of modeling the bolometric LCs of all SE SNe found by (i)PTF, using expansion velocities derived from the He I $\lambda5876$ line for SNe IIb and Ib and from the O I $\lambda7774$ line for SNe Ic. A datarelease paper for the full (i)PTF SE SN spectral sample is also in progress, which will supplement the analysis presented here (Fremling et al., in prep.).

7. Conclusions

The main conclusions of this work are as follows.

- SNe Ic show higher O I pEWs and O I velocities compared to SNe IIb and Ib (higher by ~ 50 Å and ~ 2000 km s^{-1}, at maximum light). This is inconsistent with what would be expected if low mixing was responsible for hiding He signatures in SNe Ic. SNe Ic likely lack He shells; removing the He shell will give higher velocities in the O shell for the same kinetic energy in the explosion.
- The He I $\lambda\lambda5876, 7065$ velocities at maximum light are higher in SNe Ib compared to SNe IIb. (~ 1000 km s^{-1} higher). The lack of an outer H shell in SNe Ib allow higher velocities to be reached in the He shell as the SN shock wave passes through the ejecta.
- The pEWs of the He I $\lambda\lambda5876, 7065$ absorption lines are similar past maximum light in most SNe Ib and SNe IIb. The He shells appear to be very similar among SNe IIb and Ib.
- There is an anticorrelation between He I $\lambda7065$ pEW and O I $\lambda7774$ velocity among SNe IIb and Ib. This can be interpreted as a difference in the amount of He at the time of explosion. The observed difference in the expansion rate of the ejecta around maximum light for SNe Ic and Ib imply an average He mass difference of 1.4 M$_\odot$, if all other explosion parameters are assumed to be unchanged between SNe Ic and Ib. The difference could either be on account of different starting progenitor masses that undergo a similar amount of stripping, or a continuum in the extent of stripping of the He envelope from progenitors of similar initial mass, or a combination thereof.
- Only two objects in the entire sample (PTF10qrl and iPTF15cna) show both low pEWs of He and slow velocities of either He or O . Both of these objects have very broad LCs, atypical for SE SNe. Therefore, we find that our sample does not show compelling evidence for hidden He in normal SE SNe.

References

Anderson, J. P., Habergham, S. M., James, P. A., & Hamuy, M. 2012, MNRAS, 424, 1372

Appenzeller, I., Fricke, K., Fürtig, W., et al. 1998, The Messenger, 94, 1

Arcavi, I., Gal-Yam, A., Yaron, O., et al. 2011, ApJ, 742, L18

Arnett, W. D. 1982, ApJ, 253, 785

Ben-Ami, S., Gal-Yam, A., Filippenko, A. V., et al. 2012, ApJ, 760, L33

Ben-Ami, S., Gal-Yam, A., Mazzali, P. A., et al. 2014, ApJ, 785, 37

Benn, C., Dee, K., & Agócs, T. 2008, in Proc. SPIE, Vol. 7014, Ground-based and Airborne Instrumentation for Astronomy II, 70146X

Blondin, S. & Tonry, J. L. 2007, ApJ, 666, 1024

Cano, Z. 2013, MNRAS, 434, 1098

Cao, Y., Nugent, P. E., & Kasliwal, M. M. 2016, PASP, 128, 114502

Claeys, J. S. W., de Mink, S. E., Pols, O. R., Eldridge, J. J., & Baes, M. 2011, A&A, 528, A131

Conti, P. 1976, MSRSL, 9, 193

Dessart, L. & Hillier, D. J. 2005, A&A, 439, 671

Dessart, L., Hillier, D. J., Li, C., & Woosley, S. 2012, MNRAS, 424, 2139

Dessart, L., Hillier, D. J., Woosley, S., et al. 2015, MNRAS, 453, 2189

Dessart, L., Hillier, D. J., Woosley, S., et al. 2016, MNRAS, 458, 1618

Dressler, A., Bigelow, B., Hare, T., et al. 2011, PASP, 123, 288

Drout, M. R., Soderberg, A. M., Gal-Yam, A., et al. 2011, ApJ, 741, 97

Drout, M. R., Soderberg, A. M., Mazzali, P. A., et al. 2013, ApJ, 774, 58

Ergon, M., Jerkstrand, A., Sollerman, J., et al. 2015, A&A, 580, A142

Ergon, M., Sollerman, J., Fraser, M., et al. 2014, A&A, 562, A17

Faber, S. M., Phillips, A. C., Kibrick, R. I., et al. 2003, in Proc. SPIE, Vol. 4841, Instrument Design and Performance for Optical/Infrared Ground-based Telescopes, ed. M. Iye & A. F. M. Moorwood, 1657–1669

Filippenko, A. V. 1997, ARA&A, 35, 309

Folatelli, G., Bersten, M. C., Kuncarayakti, H., et al. 2014, ApJ, 792, 7

Fremling, C., Sollerman, J., Taddia, F., Ergon, M., & Fraser, M. 2016, A&A, 593, A68

Fremling, C., Sollerman, J., Taddia, F., et al. 2014, A&A, 565, A114

Frey, L. H., Fryer, C. L., & Young, P. A. 2013, ApJ, 773, L7

Gal-Yam, A. 2016, ArXiv e-prints, 1611.09353

Gal-Yam, A., Arcavi, I., Ofek, E. O., et al. 2014, Nature, 509, 471

Guillochon, J., Parrent, J., Kelley, L. Z., & Margutti, R. 2017, ApJ, 835, 64

Hachinger, S., Mazzali, P. A., Taubenberger, S., et al. 2012, MNRAS, 422, 70

Hill, G. J., Nicklas, H. E., MacQueen, P. J., et al. 1998, in Proc. SPIE, Vol. 3355, Optical Astronomical Instrumentation, ed. S. D'Odorico, 375–386

Hook, I. M., Jørgensen, I., Allington-Smith, J. R., et al. 2004, PASP, 116, 425

Horesh, A., Kulkarni, S. R., Corsi, A., et al. 2013, ApJ, 778, 63

Iben, Jr., I. & Tutukov, A. V. 1985, ApJS, 58, 661

Jerkstrand, A., Ergon, M., Smartt, S. J., et al. 2015, A&A, 573, A12

Kasliwal, M. M., Kulkarni, S. R., Gal-Yam, A., et al. 2010, ApJ, 723, L98

Lantz, B., Aldering, G., Antilogus, P., et al. 2004, in Proc. SPIE, Vol. 5249, Optical Design and Engineering, ed. L. Mazuray, P. J. Rogers, & R. Wartmann, 146–155

Law, N. M., Kulkarni, S. R., Dekany, R. G., et al. 2009, PASP, 121, 1395

Liu, Y. & Modjaz, M. 2014, ArXiv e-prints, 1405.1437

Liu, Y.-Q., Modjaz, M., Bianco, F. B., & Graur, O. 2016, ApJ, 827, 90

Lyman, J. D., Bersier, D., James, P. A., et al. 2016, MNRAS, 457, 328

Masci, F. J., Laher, R. R., Rebbapragada, U. D., et al. 2017, PASP, 129, 014002

Matheson, T., Filippenko, A. V., Li, W., Leonard, D. C., & Shields, J. C. 2001, AJ, 121, 1648

Modjaz, M., Blondin, S., Kirshner, R. P., et al. 2014, AJ, 147, 99

Nordin, J., Östman, L., Goobar, A., et al. 2011, A&A, 526, A119

Oke, J. B., Cohen, J. G., Carr, M., et al. 1995, PASP, 107, 375

Oke, J. B. & Gunn, J. E. 1982, PASP, 94, 586

Osip, D. J., Floyd, D., & Covarrubias, R. 2008, in Proc. SPIE, Vol. 7014, Ground-based and Airborne Instrumentation for Astronomy II, 70140A

Piro, A. L. & Morozova, V. S. 2014, ApJ, 792, L11

Prentice, S. J. & Mazzali, P. A. 2017, MNRAS, 469, 2672

Prentice, S. J., Mazzali, P. A., Pian, E., et al. 2016, MNRAS, 458, 2973

Sanders, N. E., Soderberg, A. M., Levesque, E. M., et al. 2012, ApJ, 758, 132

Shivvers, I., Modjaz, M., Zheng, W., et al. 2017, PASP, 129, 054201

Smith, N. 2014, ARA&A, 52, 487

Strotjohann, N. L., Ofek, E. O., Gal-Yam, A., et al. 2015, ApJ, 811, 117

Sun, F. & Gal-Yam, A. 2017, ArXiv e-prints, 1707.02543

Taddia, F., Fremling, C., Sollerman, J., et al. 2016, A&A, 592, A89

Taddia, F., Sollerman, J., Fremling, C., et al. 2017, ArXiv e-prints

Taddia, F., Sollerman, J., Leloudas, G., et al. 2015, A&A, 574, A60

Tauris, T. M., Langer, N., Moriya, T. J., et al. 2013, ApJ, 778, L23

Yaron, O. & Gal-Yam, A. 2012, PASP, 124, 668

Yoon, S.-C. 2015, PASA, 32, 15

Yoon, S.-C., Woosley, S. E., & Langer, N. 2010, ApJ, 725, 940
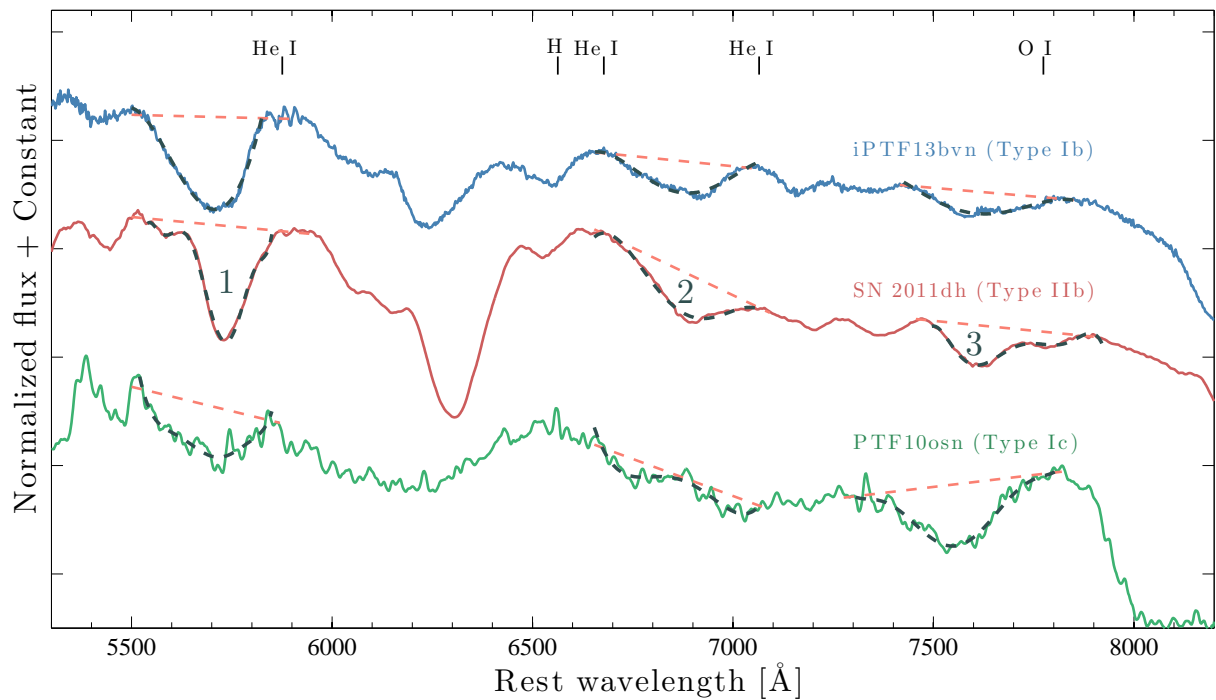
Fig. 1: Description of our pEW and expansion-velocity measurement method using spectra around peak brightness for iPTF13bvn (Type Ib, +0.5 d, upper blue line), SN 2011dh (Type IIb, +2.5 d, middle red line), and PTF10osn (Type Ic, +4.0 d, bottom green line). On the spectrum of SN 2011dh, the absorption features of He I $\lambda\lambda5876, 7065$ and O I $\lambda7774$ have been labeled with numbers. Measurements of features 1-3 have been attempted on all spectra in our sample. For SE SNe, feature 1 is typically associated with He I $\lambda5876$, feature 2 with He I $\lambda7065$, and feature 3 with O I $\lambda7774$, although other elements also contribute to these features. Dashed red lines indicate pseudo-continuum estimates (first-order polynomial fits) for features 1-3 resulting from our measurement scheme (Sect. 3). We calculate pEWs (e.g., Fig. 2) between the endpoints of these continuum estimates using Eq. 1. Velocity estimates are obtained by locating the minima of polynomial fits between the pseudo-continuum endpoints (order 4-7, dashed black lines). If a spectral feature is ambiguous, and has several minima within a similar range as shown for feature 2 in the spectrum of PTF10osn, we set the velocity estimate to be undefined but still calculate the pEW. Wavelengths have been shifted to the rest frame, and the spectra have been normalized and shifted by a constant for clarity.
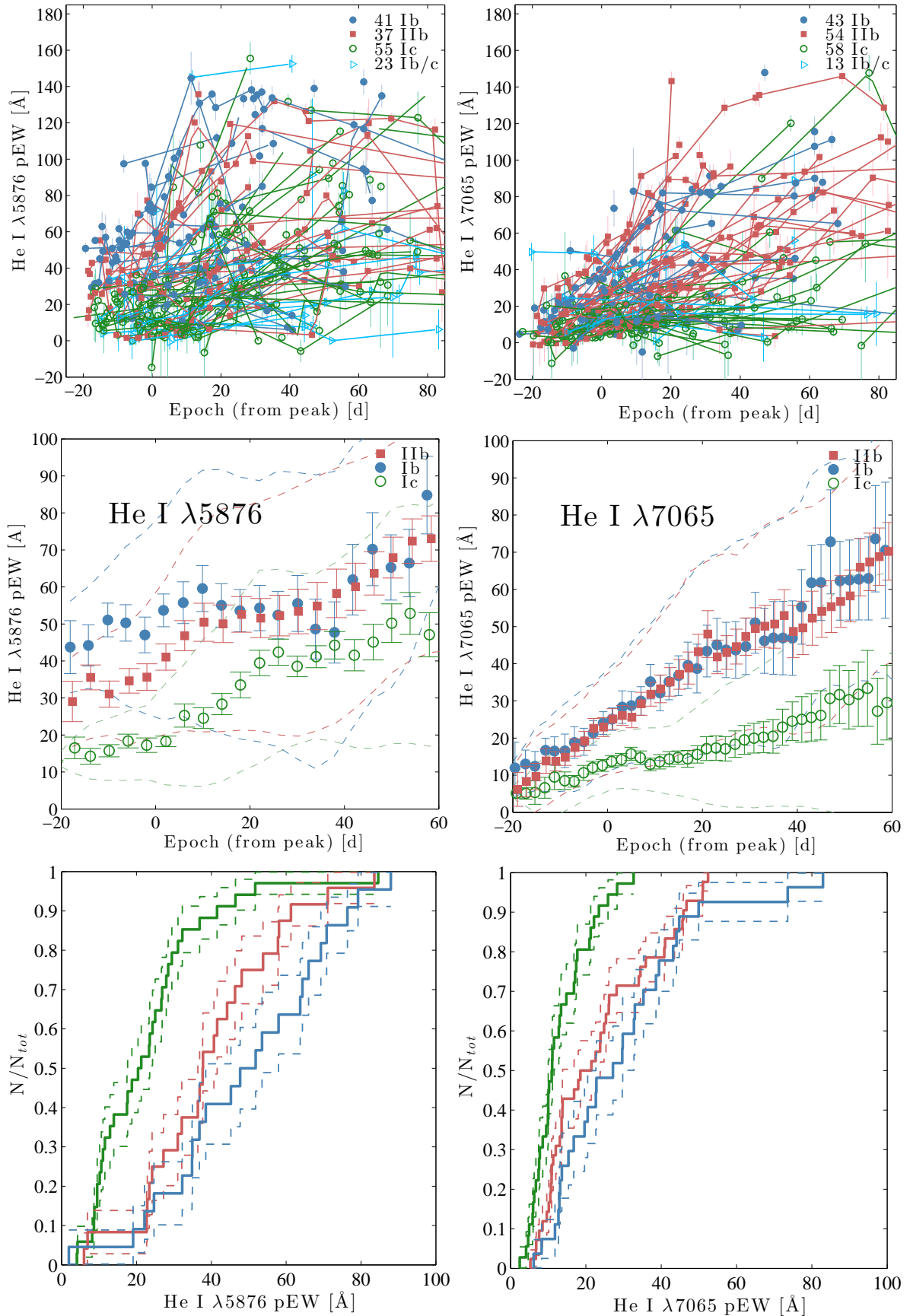
Fig. 2: Absorption strengths of He I λ5876 (left panels) and He I λ7065 (right panels). The top panels show individual measurements, with multiple measurements of the same SN connected by solid lines. The middle panels show averages of the SE SN subtypes, with error bars representing the standard deviation of the mean. Dashed lines outline the standard deviations of the samples for each subtype in matching color. The bottom panels show CDFs measured between −10 and +10 d
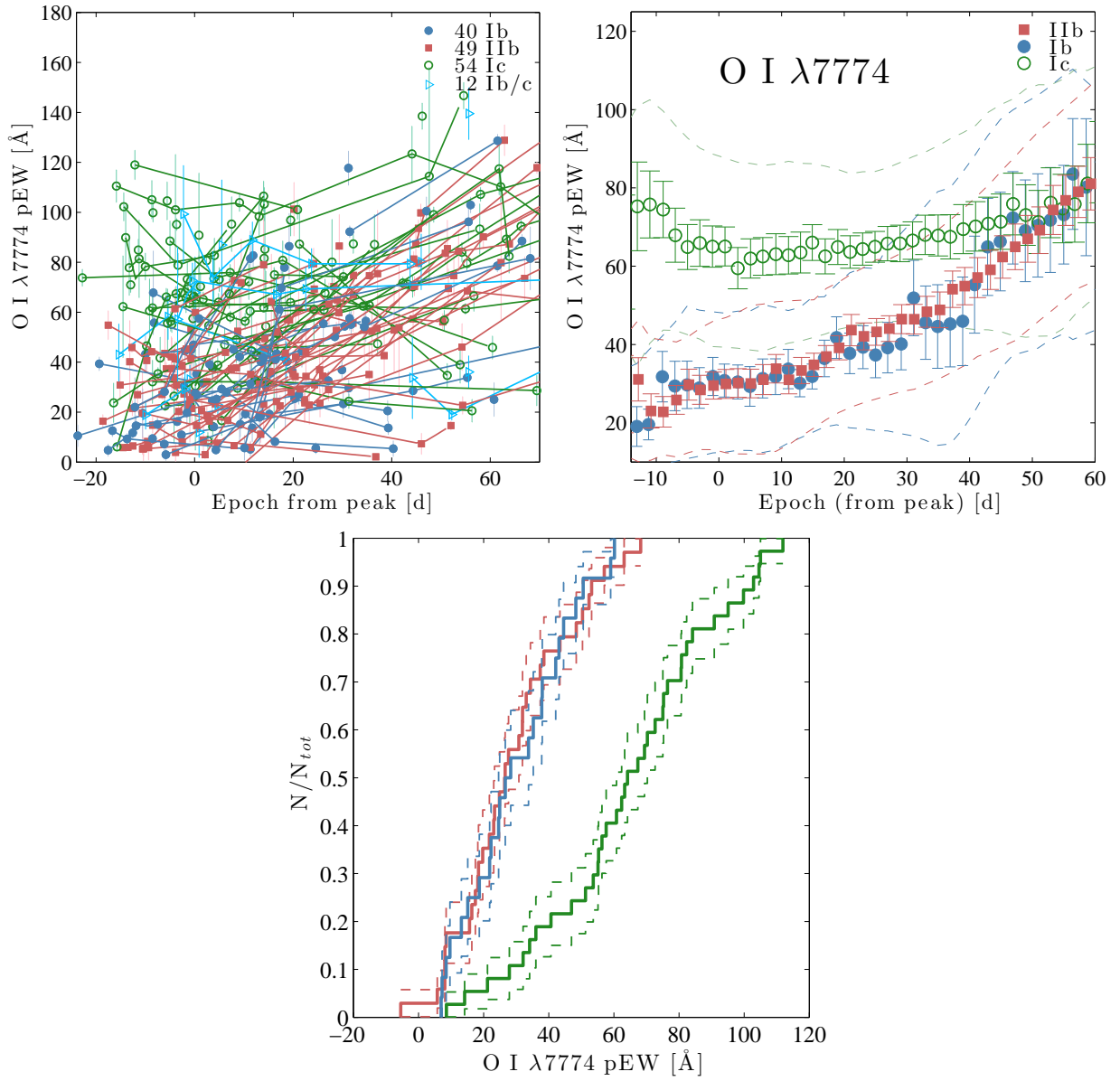
Fig. 3: Absorption strengths of O I λ7774 (top panels). The top-left panel shows individual measurements, with multiple measurements of the same SN connected by solid lines. The top-right panel shows the averages of the SE SN subtypes, with error bars representing the standard deviation of the mean. Dashed lines outline the standard deviations of the samples for each subtype in matching color. The bottom panel shows CDFs measured between -10 and $+10$ d.
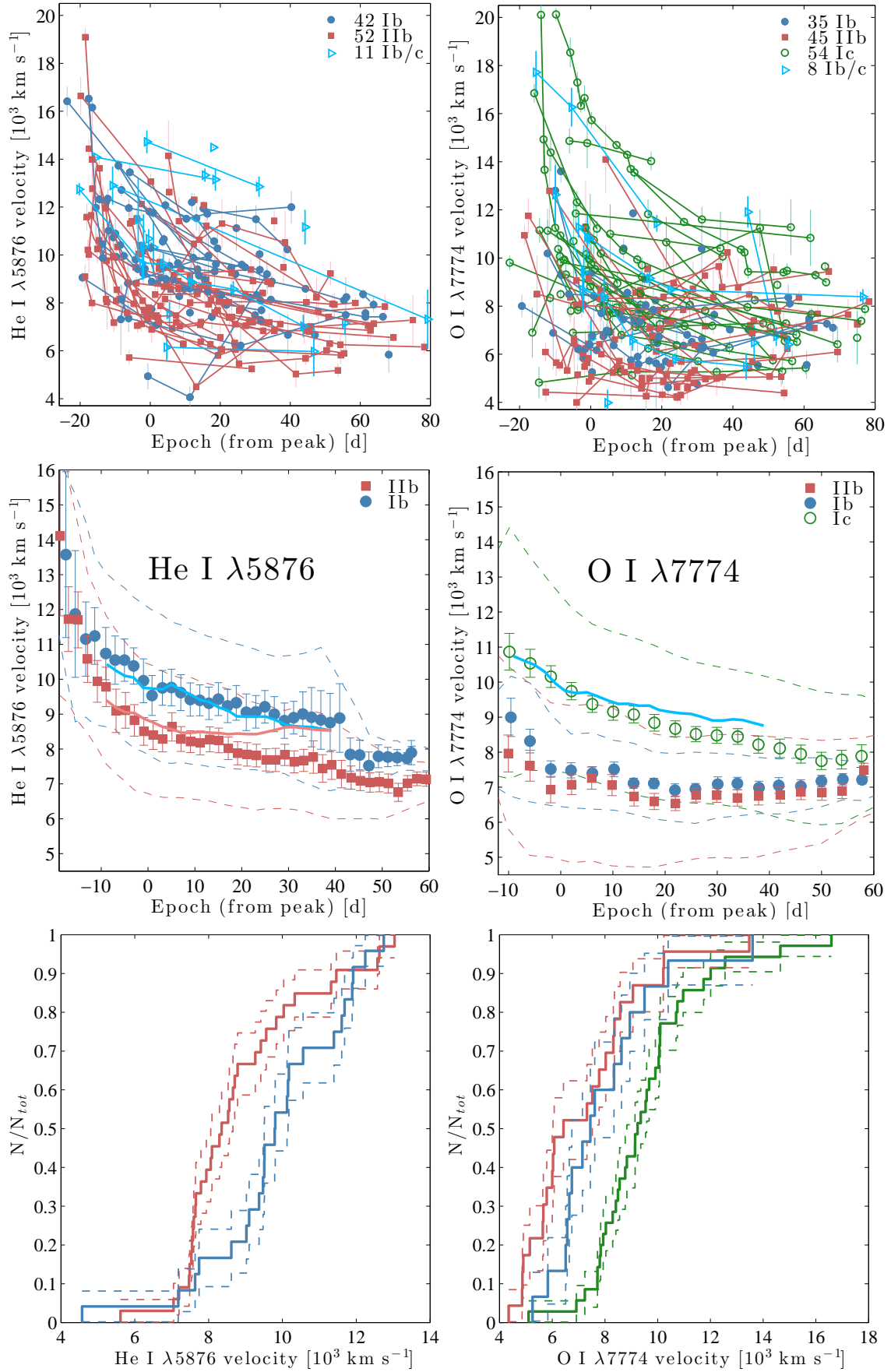
Fig. 4: Velocities of He I λ5876 (left panels) and O I λ7774 (right panels). The top panels show individual measurements, with measurements of the same SN connected by solid lines. The middle panels show averages of the SE subtypes, with error bars representing the standard deviation of the mean. Dashed lines outline the standard deviations of the samples for each subtype in matching color. Average velocities derived from He I λ7065 are shown as thick solid lines (Type Ib in blue and Type IIb in red) in the middle-left panel. The average He I λ5876 velocity of Type Ib SNe is shown as a thick solid line in the middle-right panel. The bottom panels show CDFs measured between −10 and +10 d for each subtype.
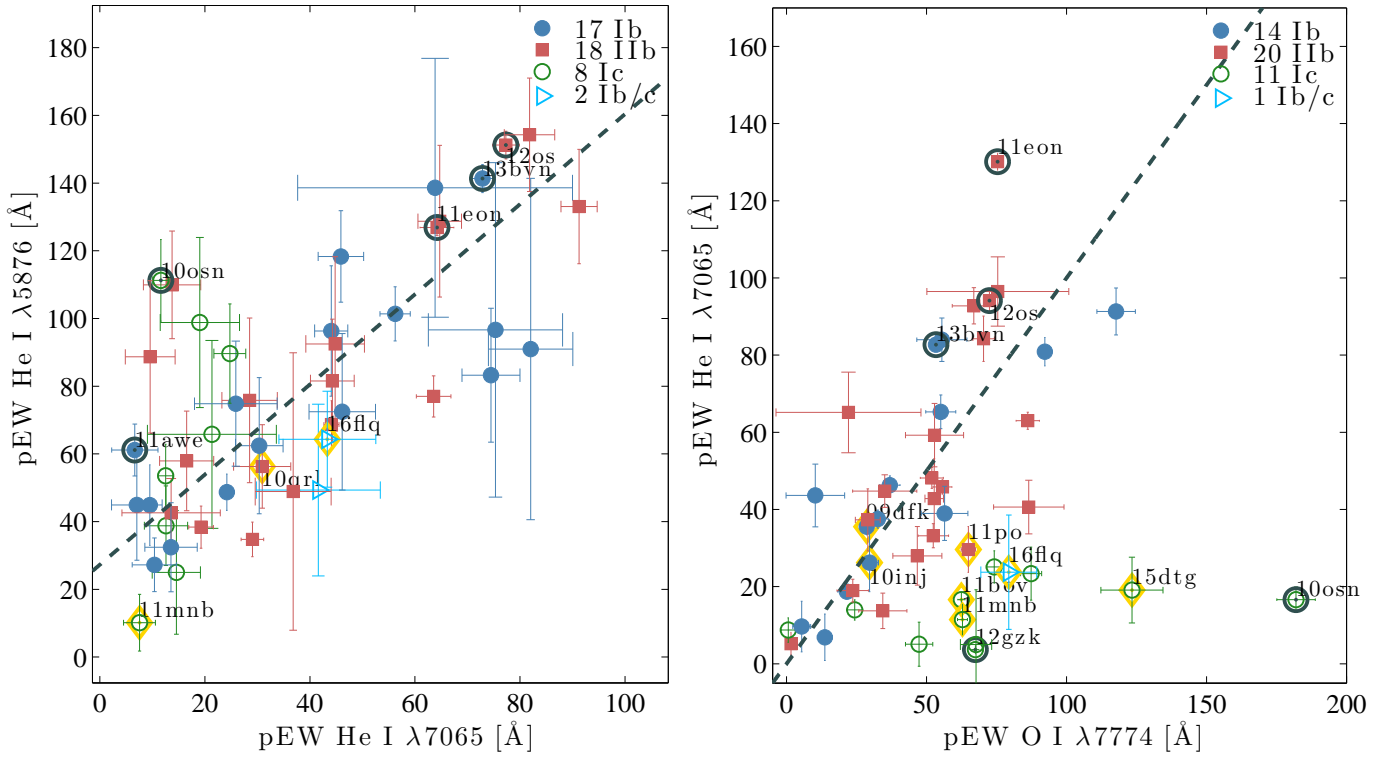
Fig. 5: Scatter plots of average pEW values for the SE SNe in our sample. He I $\lambda7065$ vs. He I $\lambda5876$ calculated between +10 d and +20 d, along with the best-fit relation $\text{pEW}_{\lambda5876} = 30 + 1.3 \times \text{pEW}_{\lambda7065}$ as a dashed line (left panel). O I $\lambda7774$ vs. He I $\lambda7065$ at +25 d to +45 d with the best-fit relation $\text{pEW}_{\lambda7065} = 1.0 \times \text{pEW}_{\lambda7774}$ (right panel). An illustrative set of SNe have been labeled by their abbreviated (i)PTF names in both panels. Yellow diamonds indicate all objects showing very broad LCs.
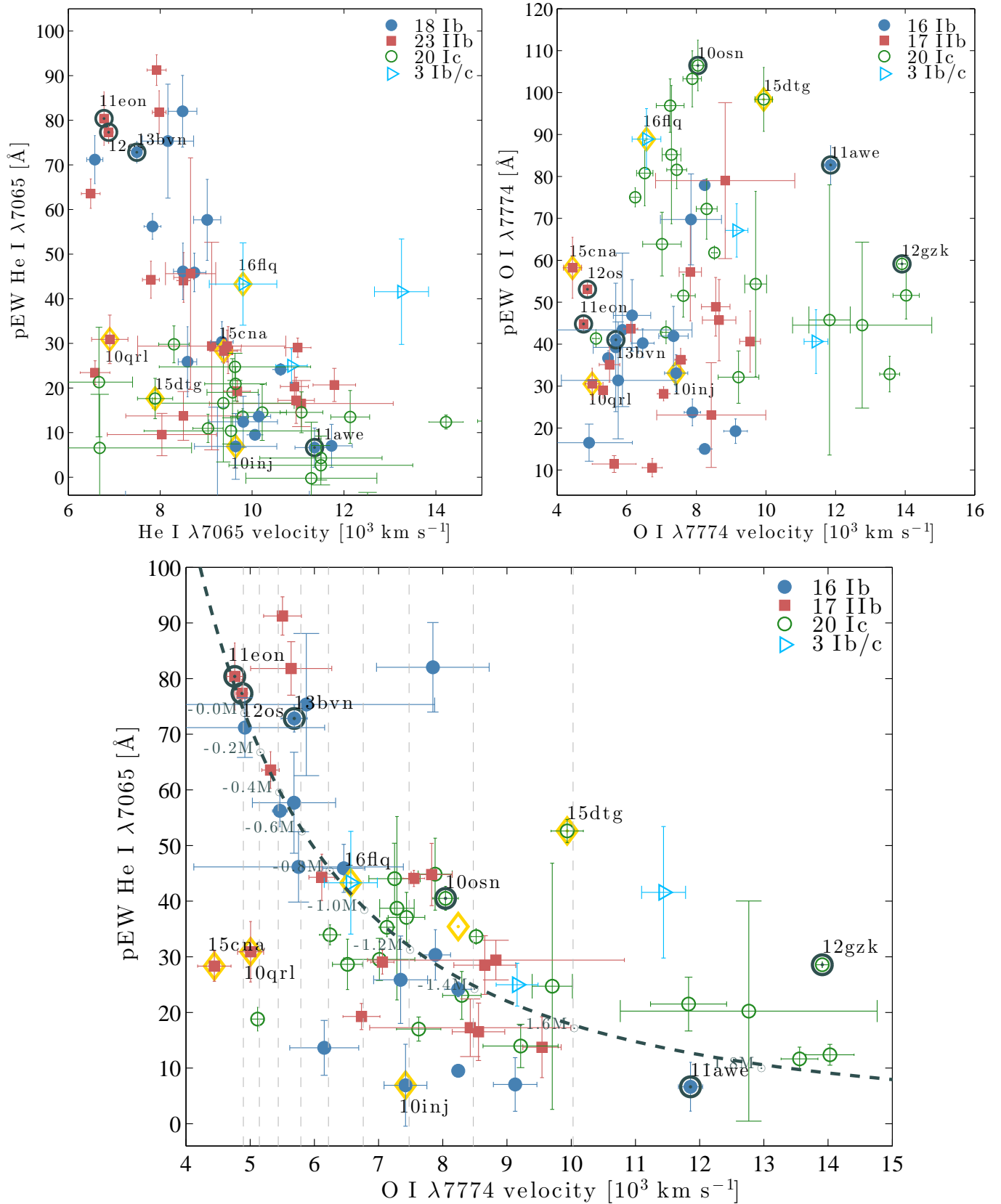
Fig. 6: Average pEW vs. velocity of He I $\lambda7065$ between +10 and +20 d (top-left panel). Average pEW vs. velocity of O I $\lambda7774$ between +10 and +20 d (top-right panel). Average pEW of He I $\lambda7065$ vs. velocity of O I $\lambda7774$ between +10 d and +20 d for SNe IIb and Ib, and the pEW of O I $\lambda7774$ scaled down by a factor of 2.2 vs. O I $\lambda7774$ velocity for SNe Ic (bottom panel). An illustrative set of SNe have been labeled by their abbreviated (i)PTF names. Yellow diamonds indicate all objects showing very broad LCs. In the bottom panel the thick dashed black line indicates the best-fit relation pEW$\propto v^{-2}$. The dashed vertical lines indicate the velocity increase expected from the Arnett (1982) model by removing 0.2 $M_\odot$ of material from the ejecta (the He envelope) for each line from left to right (mass-difference labels follow the thick dashed black line). The model has been scaled, so that the O I $\lambda7774$ velocity predicted for a total ejecta mass of 2.1 $M_\odot$ is 4900 km s^{-1}, to match the observed velocities of SN 2011dh (PTF11eon) and PTF12os. Two SNe IIb (iPTF15cna and PTF10qrl) are strong outliers from the fitted trend. These two SNe have very broad LCs and low O I $\lambda7774$ velocities (see Sect. 6 for further discussion).

Table 2: Spectral log for the (i)PTF SE SN sample.

SN	Type	Phase [rest-frame days from peak]	Redshift z	$MW_{E_{B-V}}$ [mag]
09awk	Ib	24 25	0.062	0.02
09dah	IIb	-15 -13 19 24 25 44 50 55	0.024	0.05
09dfk	Ib	-3 24 44 55	0.016	0.05
09dh	Ic	-6 -1 11 17	0.070	0.02
09dha	Ib	9	0.030	0.02
09dsj	IIb	-1	0.135	0.02
09dxv	IIb	-4 2 21 32	0.032	0.15
09dzt	Ic	1	0.087	0.08
09fae	IIb	5	0.067	0.03
09fsr	Ib	18	0.008	0.10
09gxq	IIb	16	0.038	0.04
09gyp	IIb	-9	0.046	0.02
09hnq	IIb	-6	0.027	0.09
09iqd	Ic	-5	0.034	0.05
09ism	IIb	4 32	0.030	0.06
09ps	Ic	4	0.106	0.01
09ut	Ib/c	0	0.042	0.03
10abck	Ib	-2 4	0.014	0.11
10acbu	Ib	46 77 96	0.010	0.01
10acff	Ib	-4	0.060	0.02
10acgq	Ib	12 41	0.105	0.02
10bhu	Ic	6	0.036	0.01
10bip	Ic	14	0.051	0.02
10cxx	IIb	38 50	0.034	0.04
10eqi	Ib	30	0.030	0.02
10fbv	Ib	0	0.056	0.03
10feq	Ib	-8 19	0.028	0.03
10fia	Ib	4	0.039	0.05
10fmr	IIb	45 46 63	0.020	0.01
10fmx	Ic	21 51 80	0.047	0.01
10fqg	IIb	0	0.028	0.03
10gmf	IIb	-13 -2	0.040	0.02
10hfe	Ic	-7 11	0.049	0.02
10hie	Ic	16 37	0.067	0.05
10in	IIb	22 51	0.070	0.05
10inj	Ib	-24 12 31 68 93	0.066	0.01
10kui	Ib	-19 2	0.021	0.01
10lbo	Ic	-8	0.053	0.01
10ood	Ic	4 5 9 57	0.059	0.14
10osn	Ic	-14 -13 -10 4 14 39	0.038	0.04
10pbi	Ib	15 30 39	0.048	0.07
10pzp	IIb	10	0.081	0.02
10qif	Ib	0 35	0.064	0.06
10qqd	Ic	0 3 28	0.081	0.08
10qrl	IIb	-11 14	0.040	0.07
10svt	Ic	75	0.031	0.10
10tqi	Ic	-1 0 35	0.038	0.03
10tqv	Ic	5 36 65	0.080	0.06
10tud	IIb	6	0.094	0.02
10tzh	IIb	-18 17 20	0.034	0.02
10vns	IIb	34	0.040	0.05
10vnv	Ib	47	0.015	0.10
10wal	Ic	12 41	0.029	0.03
10wg	Ib/c	5	0.090	0.01
10xfl	IIb	-1 13	0.050	0.09
10xik	Ic	19 63	0.071	0.08
10xjr	Ib	31	0.030	0.03
10yow	Ic	4 18 19 22 48 54	0.025	0.09
10zcn	Ic	14	0.020	0.08
11awe	Ib	12	0.055	0.02
11bli	Ib/c	5 47	0.030	0.01
11bov	Ic	-23 7 34 85	0.022	0.03
11dhf	IIb	-4 8	0.028	0.02

Table 2 – continued from previous page

SN	Type	Phase [rest-frame days from peak]	Redshift z	MW$_{E_{B-V}}$ [mag]
11dlg	IIb	9	0.062	0.03
11eon	IIb	-19 -18 -15 -14 -13 -10 2 7 8 14 35 44 45 69 81 83 91	0.002	0.03
11gcj	Ib/c	7 13	0.148	0.01
11hyg	Ic	13 49	0.030	0.05
11ilr	Ib	20 22 32	0.037	0.18
11ixk	Ic	2	0.021	0.01
11izq	Ib	5 18	0.062	0.01
11izr	Ib/c	-10 44 52 83	0.075	0.03
11jgj	Ic	-16 -7 17	0.040	0.03
11kaa	Ib	5 13 15	0.040	0.02
11klg	Ic	-14 -3 48 55	0.027	0.08
11lmn	Ib/c	-5 17	0.090	0.04
11mnb	Ic	-15 8 35 60 97	0.060	0.02
11mwk	Ib/c	-1 31	0.121	0.05
11pdj	IIb	-19 14 36 37 48 67	0.024	0.07
11pnq	Ib/c	-15 -5 10 17 19	0.074	0.04
11po	IIb	-6 29	0.070	0.05
11prr	IIb	-9 -3 12 13 20 38 40 41 47 51	0.053	0.12
11qcj	Ic	9 10 12 31 56 66	0.028	0.01
11qiq	Ib	-17 -14 -10 8 11 20 39	0.032	0.06
11qju	IIb	23 54 78	0.028	0.01
11rka	Ic	-1 31 55	0.074	0.03
11rkm	IIb	4 8 26 34 88	0.065	0.01
12bwq	Ib	-10 -2 3	0.040	0.01
12cde	Ib/c	18 46	0.013	0.01
12cjy	Ic	0 14	0.044	0.01
12dcp	Ic	-9 0 5 18 58	0.031	0.02
12dtf	Ic	-9 14 69	0.061	0.03
12eaw	Ib	-8 -6 17	0.029	0.01
12eje	IIb	9 14	0.078	0.01
12fes	Ib	-12 21	0.036	0.04
12fgw	Ic	10	0.055	0.03
12fhz	IIb	10 43 44 75	0.099	0.03
12fxj	IIb	15	0.015	0.05
12gpn	IIb	-5 -3 3 7 29	0.022	0.03
12gps	Ib	-1 11 33	0.016	0.02
12gty	Ic	-11 -6	0.176	0.06
12gvr	Ib/c	1	0.056	0.03
12gzk	Ic	-16 -15 -12 -11 -10 -6 -4 -3 -2 0 7 10 11 26 42 43 44 54 55 63 66 86 94 95	0.014	0.04
12hni	Ic	-5 5	0.107	0.05
12hvv	Ic	-12 21	0.029	0.07
12iqw	IIb	-17 13 37	0.027	0.19
12jaa	IIb	-20 0 24	0.024	0.08
12jxd	Ic	14 55 58 86	0.025	0.03
12ktu	Ic	-9 19 26	0.031	0.06
12lpo	Ib/c	*	0.004	0.03
12ltw	Ib	9 23 26	0.060	0.07
12lvt	Ib	61	0.012	0.06
12mfx	Ib	0 27	0.113	0.06
12os	IIb	-13 -10 -9 -5 -2 -1 2 6 14 19 24 27 28 29 32 93 94	0.005	0.04
13ab	Ic	-5 -1 8	0.048	0.02
13aby	IIb	-18 -15 -9 -4 19 51 64 83	0.018	0.01
13ajn	IIb	-22 -21 -17 2 34	0.030	0.04
13aoo	IIb	-4 2 37	0.036	0.01
13aot	Ic	66 96	0.019	0.01
13ast	IIb	-10 -7 -4 5 17 20 23 45 53 59 81 83	0.026	0.01
13blq	IIb	-1 35	0.088	0.02
13bvn	Ib	-18 -17 -16 -15 -14 -13 -11 -9 -8 -4 -2 0 4 6 13 16 28 30 31 34 61 66	0.004	0.04
13cab	Ib	4	0.030	0.06
13cbf	Ic	51	0.039	0.06
13ccj	Ic	52	0.019	0.05
13cr	IIb	25	0.059	0.02
13cuv	Ic	1	0.049	0.06
13dht	Ic	-11	0.040	0.07

Table 2 – continued from previous page

SN	Type	Phase [rest-frame days from peak]	Redshift z	MW$_{E_{B-V}}$ [mag]
13djf	Ic	-13 -11 2	0.021	0.07
13doq	Ib	-4	0.072	0.12
13dug	Ib	31 61	0.005	0.02
13ebs	IIb	11 17	0.027	0.02
13edf	Ib	18 56	0.027	0.04
13nu	IIb	-12 9 18 45 72	0.026	0.01
13v	IIb	29	0.062	0.01
14aag	IIb	1 13	0.030	0.03
14ait	Ib/c	56	0.039	0.02
14apl	Ic	14	0.036	0.03
14atc	IIb	5 8 23 27 62 90	0.068	0.01
14bas	IIb	-11 0 20 54 85	0.039	0.03
14bpy	Ic	-4 62 64	0.045	0.04
14cyn	Ib	-8 -6 26 56	0.134	0.03
14fuz	Ib/c	-10 -2	0.044	0.02
14gao	Ic	-4	0.018	0.07
14gjv	Ib	11	0.018	0.02
14igl	Ib	-6 13 19	0.039	0.01
14ikn	IIb	-12 -10 16	0.020	0.08
14jhf	Ib/c	-11 79	0.053	0.02
14ur	Ic	32	0.008	0.03
14va	Ib/c	*	0.006	0.02
14ym	Ic	24	0.031	0.04
15acp	Ic	-15 -14 2 12 36	0.138	0.01
15acr	IIb	-18 -17 -3 9	0.061	0.01
15adv	Ib	4 10 16 40	0.045	0.02
15afv	Ib	*	0.003	0.08
15afw	IIb	-19 -17 -7 -5 1 7 11 21 22	0.008	0.03
15aiw	Ib	-12 -6 1	0.067	0.01
15cam	IIb	-1 16 46 52	0.028	0.13
15cna	IIb	16 17 23 42 54 83	0.060	0.11
15cpq	Ib/c	-3 0 10 17 23 77	0.066	0.02
15dh	Ic	-5	0.031	0.07
15dpa	IIb	-4	0.057	0.02
15dqb	Ib	61 64	0.043	0.08
15dtg	Ic	-17 -16 -4 5 9 13 44 62 76	0.052	0.05
15dvg	Ib	-9 4 8 14	0.047	0.04
15eoc	IIb	3 20	0.007	1.16
15eqv	IIb	*	0.005	0.02
15fhl	Ic	16 30	0.044	0.03
15n	Ib	10 17 68	0.038	0.03
16ahq	Ib	56	0.004	0.01
16bfy	Ic	7	0.033	0.02
16flq	Ib/c	-20 -2 4 12 24 44	0.060	0.02
16he	IIb	-4 14	0.031	0.02
16hgp	Ic	-20 -9	0.079	0.04

Note. — Spectra were obtained using the following telescopes and instruments: Keck I/LRIS (Oke et al. 1995), Keck II/DEIMOS (Faber et al. 2003), P200/DBSP (Oke & Gunn 1982), P60/SEDM, Gemini N/GMOS (Hook et al. 2004), Gemini S/GMOS-S, WHT/ACAM (Benn et al. 2008), WHT/ISIS, NOT/ALFOSC, ARC 3.5m/DIS, Lick 3m/KAST, FTN/FLOYDS, FTS/FLOYDS, DCT/DeVeny/LMI, GTC/OSIRIS, HET/LRS (Hill et al. 1998), KPNO 4m/RCSpec, Magellan I/IMACS (Dressler et al. 2011), Magellan II/LDSS3 (Osip et al. 2008), SALT/RSS, TNG/DOLORES, UH88/SNIFS (Lantz et al. 2004), VLT/FORS2 (Appenzeller et al. 1998), Wise 1m/FOSC.

Note 2. — For objects with a * in the epoch field it was impossible to determine the time of maximum light from their LCs. We have classified these objects based on spectra obtained by the (i)PTF, but they are not included in any further analysis.